



# The Closure Relations in Optical Afterglow of Gamma-Ray Bursts

M. G. Dainotti<sup>1,2,3</sup> , D. Levine<sup>4</sup> , N. Fraija<sup>5</sup> , D. Warren<sup>6</sup> , and S. Sourav<sup>7</sup> <sup>1</sup> National Astronomical Observatory of Japan, Tokyo, Japan; [maria.dainotti@nao.ac.jp](mailto:maria.dainotti@nao.ac.jp)<sup>2</sup> Sokendai University, Japan<sup>3</sup> Space Science Institute, Boulder, Colorado, USA<sup>4</sup> Department of Astronomy, University of Maryland, College Park, MD 20742, USA<sup>5</sup> Instituto de Astronomia, Universidad Nacional Autónoma de México<sup>6</sup> RIKEN Interdisciplinary Theoretical and Mathematical Sciences Program (iTHEMS), Wakō, Saitama, 351-0198 Japan<sup>7</sup> Department of Data Science and Engineering, Indian Institute of Science Education and Research, Bhopal, Madhya Pradesh, India

Received 2022 July 11; revised 2022 September 20; accepted 2022 September 30; published 2022 December 1

## Abstract

Gamma-ray bursts (GRBs) are extremely high-energy events that can be observed at very high redshift. In addition to  $\gamma$  rays, they can emit in X-ray, optical, and sometimes radio wavelengths. Here, following the approach in Srinivasaragavan et al.; Dainotti et al.; and Dainotti et al., we consider 82 GRBs from Dainotti et al. that have been observed in optical wavelengths and fitted with a broken power law. We consider the relations between the spectral and temporal indices (closure relations; CRs) according to the synchrotron forward-shock model evolving in the constant-density interstellar medium (ISM;  $k = 0$ ) and the stellar wind environment ( $k = 2$ ) in both slow- and fast-cooling regimes, where the density profile is defined as  $n \propto r^{-k}$ . We find the  $\nu > \max\{\nu_c, \nu_m\}$  regime is most favored, where  $\nu_c$  and  $\nu_m$  are the cooling and characteristic frequencies, respectively. Finally, we test the 2D Dainotti correlation between the rest-frame end time of the plateau and the luminosity at that time on GRBs that fulfill the most-favored CRs. When we compare the intrinsic scatter  $\sigma_{int}$  of those 2D correlations to the scatter presented in Dainotti et al., we see the scatters of our correlations generally agree with the previous values within  $1\sigma$ , both before and after correction for selection bias. This new information has helped us to pinpoint subsamples of GRBs with features that could drive the GRB emission mechanism, and eventually allow for GRBs to be used as standard candles.

*Unified Astronomy Thesaurus concepts:* Gamma-ray bursts (629)

## 1. Introduction

Gamma-ray bursts (GRBs) are very high-energy bursts that can emit in  $\gamma$ -rays, X-rays, optical, and radio wavelengths. They are of significant interest as their high luminosities allow them to be observed at great distances, including redshifts up to  $z = 10$  (Cucchiara et al. 2011). This has sparked interest in using GRBs as standard candles, for a better method of probing cosmological distances.

GRBs undergo two phases: the “prompt” episode, which is the initial explosion seen in  $\gamma$ -rays, X-rays, and sometimes optical wavelengths where the phase of fast rise and exponential decay is visible, and the longer-lasting “afterglow” emission, which can be observed in X-ray, optical, and sometimes radio wavelengths. Beginning in 2004, the Neil Gehrels Swift Observatory (hereafter Swift) has observed many GRB afterglows at a wide range of redshifts, luminosities, and durations. To date, Swift has observed 1543 GRBs, which includes 1301 UV and optical observations supplemented with UVOT (UltraViolet and Optical Telescope). This makes optical afterglow observations the second-most frequently recorded, following 1347 X-ray observations with the X-ray Telescope (XRT).<sup>8</sup> The multiwavelength observations from Swift have been essential to GRB population studies, as they allow for

comparison among wavelengths and classes that give vital insight into the physics of GRBs.

GRB afterglows are thought to be caused by the external forward shock (FS), which is when the relativistic outflow from the progenitor impacts the external medium (Paczynski & Rhoads 1993; Katz & Piran 1997; Meszaros & Rees 1997; Sari & Piran 1999; Kumar & Piran 2000; Kumar & Duran 2010). The FS is an integral part of the widely accepted standard fireball model (Sari & Piran 1995, 1999; Sari et al. 1996; Kumar & Piran 2000; Granot & Sari 2002; Zhang et al. 2006a), which describes the emission of the GRB in both the prompt and afterglow phases. The fireball model can be tested with closure relations, or relations between the spectral and temporal indices of a GRB. These typically aim to determine whether observations of a GRB agree with expectations of two environments—the constant-density interstellar medium (ISM), which is generally assumed to be the environment for short GRBs (SGRB), or the stellar wind environment, which is ejected during the collapse of massive stars (Meszaros & Rees 1994; Daigne & Mochkovitch 1998; Chevalier & Li 2000; Panaitescu & Kumar 2000).

Studies of closure relations have previously been conducted in high energy, X-rays, optical, and radio. Extensive sets of closure relations (CRs) have been presented in studies such as Zhang & Mészáros (2004); Racusin et al. (2009); Gao et al. (2013); Lü et al. (2017); Tak et al. (2019). In high energy, Tak et al. (2019) studied a sample of 59 GRBs observed by Fermi-LAT (Large Area Telescope) in both a constant-density ISM and wind environment. They found that their sample is well described by the standard fireball model, and their most-preferred environments are those that involve Slow Cooling

<sup>8</sup> [https://swift.gsfc.nasa.gov/archive/grb\\_table/stats/](https://swift.gsfc.nasa.gov/archive/grb_table/stats/)



(SC-only) or both slow and fast cooling in the ISM environment. Dainotti et al. (2022, submitted) also considered high-energy emission in a sample of 86 GRBs observed by Fermi-LAT and similarly found that their sample can be well described by the standard fireball model with a preference for SC-only or slow- and fast-cooling environments.

In X-rays, a study by Racusin et al. (2009) considered CRs both with and without energy injection for a sample of 230 X-ray afterglows. They found that the CRs are satisfied by a majority of their sample and the standard fireball model describes their sample well. They also found a preference for the ISM environment over the wind environment. A more recent study by Srinivasaragavan et al. (2020) considered a sample of 455 X-ray GRB afterglows after the plateau phase on CRs without energy injection and again found that their sample fit the standard fireball model and prefers SC-only regimes, with no strong preference between an ISM or wind environment. Dainotti et al. (2021b) considered the same sample, but within the plateau region on CRs with energy injection, and found a particular preference for an SC, wind environment, with the majority of their sample satisfying at least one CR. Studies of synchrotron self-Compton emission in X-rays reveal that CRs in X-rays can mimic the traditional power-law decay phase if thermal electrons are present (Warren et al. 2022).

In optical, a prior study by Oates et al. (2012) considered 48 GRBs observed by Swift and found that their sample follows the basic standard fireball model according to the CRs. They tested three CRs, one in a wind environment, one in an ISM environment, and one independent of an external environment, and found low rates of satisfaction for each relation. Other studies include both X-ray and optical wavelengths, such as Wang et al. (2015), which considered a sample of 85 GRBs observed with Swift and found 45 GRBs that were well described by the standard fireball model, with an additional 37 GRBs described at least in part by the fireball model. Fukushima et al. (2017) considered numerical models of X-ray and optical light curves in an ISM environment in both fast- and slow-cooling regimes, applying their model to GRB 130427A. They found discrepancies in the decay indices for X-ray and optical wavelengths, suggesting that a more complicated model is needed to accurately describe the GRB afterglow. Jelínek et al. (2022) studied the optical afterglow of long GRB 190919B and found the behavior of the afterglow consistent with an SC, ISM environment. Some studies have considered both optical and X-ray afterglows of single GRBs—Afonso et al. (2011) studied GRB 050502B to decipher possible correlations between optical and X-ray data and found both the optical and X-ray afterglows satisfy SC relations for both ISM and wind, while Starling et al. (2009) studied GRB 080721 and found the afterglow inconsistent with expectations of the standard fireball model.

Though it is the least frequently observed afterglow, recent studies have considered CRs in radio wavelengths. Kangas & Fruchter (2021) examined a sample of 21 radio light curves (LCs) and found their sample does not fulfill the CRs well, indicating their sample is largely incompatible with the standard fireball model, as the behavior of the radio LCs does not agree with the behavior in the corresponding X-ray and optical LCs. Misra et al. (2021) studied the afterglow of GRB 190114C in multiple wavelengths, including X-ray, optical, and radio, and found the X-ray and radio LCs are incompatible with the standard model. For instance, Fraija et al. (2019a, 2019b)

found that synchrotron self-Compton (SSC) emissions from reverse and forward-shock regions are required to successfully describe the afterglow observations of GRB 190114C. GRB afterglows at low energy are especially susceptible to the presence of thermal electrons in the particle distribution (Ressler & Laskar 2017; Warren et al. 2022), the tension between observations and the traditional model for afterglows may point to a revised understanding of how astrophysical shocks energize the particles that they sweep up. On the other hand, Fraija et al. (2022) considered the Second Gamma-ray Burst LAT Catalog (2FLGC) and SSC afterglow model evolving in a constant and stratified medium, and when the progenitor injects continuous energy into the blastwave. They found that the CRs of the SSC model can satisfy a significant fraction of bursts in the 2FLGC that cannot be interpreted in the synchrotron afterglow scenario.

Previous studies have shown that Swift X-ray LCs have complex features beyond a simple power-law decay (Tagliaferri et al. 2005; Nousek et al. 2006; O’Brien et al. 2006; Zhang et al. 2006b, 2007a, 2007b, 2007c; Sakamoto et al. 2007; Zhang 2007; Zhao et al. 2019; Fraija et al. 2019c). A plateau feature or a flattening of the LC immediately following the prompt emission and preceding the afterglow decay, has been found in all wavelengths of the GRB afterglow, including X-ray (Nousek et al. 2006; O’Brien et al. 2006; Zhang et al. 2006b; Sakamoto et al. 2007; Evans et al. 2009), optical (Dainotti et al. 2020b, 2022a), and radio (Levine et al. 2022) wavelengths. These plateaus typically last from on the order of  $10^2$ – $10^5$  s, and are thought to result from continuous energy injection from a central engine (Dai & Lu 1998; Rees & Mészáros 1998; Sari & Mészáros 2000; Zhang & Mészáros 2001; Zhang et al. 2006b; Liang et al. 2007)—either the fall-back accretion of matter onto a black hole (Kumar et al. 2008; Cannizzo & Gehrels 2009; Cannizzo et al. 2011; Beniamini et al. 2017; Metzger et al. 2018) or the spin-down luminosity from a newborn magnetar (Zhang & Mészáros 2001; Toma et al. 2007; Troja et al. 2007; Dall’Osso et al. 2011; Rowlinson et al. 2013, 2014; Rea et al. 2015; Beniamini & Mochkovitch 2017; Metzger et al. 2018; Stratta et al. 2018; Fraija et al. 2021).

This plateau has been used to develop a correlation between the rest-frame end time of the plateau in X-rays and its correspondent luminosity at that time, called the 2D Dainotti correlation in X-rays (Dainotti et al. 2008, 2010, 2011, 2013b, 2017a; Del Vecchio et al. 2016; Zhang et al. 2018). This correlation has been extended to optical (Dainotti et al. 2020b, 2022a) and radio afterglows (Levine et al. 2022). It has been proposed as a possible method of standardizing the varied sample of GRBs to use it as a cosmological tool (Cardone et al. 2009, 2010; Dainotti et al. 2013a, 2022b, 2022c, 2022d; Postnikov et al. 2014; Cao et al. 2022a, 2022b). Dainotti et al. (2016); Dainotti & Del Vecchio (2017); Dainotti et al. (2020a, 2022a) analyze an extension of this 2D correlation to the 3D fundamental plane both in X-rays and optical, which describes a correlation between the rest-frame end time of the plateau, the luminosity at that time, and the peak prompt luminosity.

Generally, interpreting GRB afterglows in optical wavelengths presents a more complicated problem than other wavelengths. In addition to the forward shock, the afterglow could involve a possible reverse shock (material that propagates back into the GRB shell; Sari & Piran (1995)), or an association with a supernova—both of which readily emit at optical wavelengths. This makes testing CRs on optical GRBs

difficult, as the CRs test the afterglow resulting specifically from the FS and may not be able to accurately describe emissions resulting from these other physical phenomena. Nevertheless, in this study, we aim to determine whether a sample of optical GRB afterglows can be accurately described by the standard fireball model through a set of CRs. We also aim to determine if GRBs classified as agreeing with a particular environment can follow the 2D luminosity–time correlation and whether those correlations have a reduced scatter from the optical 2D correlation found in the previous literature.

This paper is organized as follows: in Section 2 we discuss the sample used for this analysis, and in Section 3 we discuss our methodology, both in terms of the CRs (Section 3.1) and the luminosity–time correlation (Section 3.2). In Section 4.1, we present the results of the CR analysis in optical, and in Section 4.2, we compare the results in optical to results obtained in other wavelengths. In Section 4.3, we present the results of the correlation analysis with preferred CRs. Finally, in Section 5, we discuss our results and present our conclusions.

## 2. Data Sample and Fitting

We take our sample of 82 GRBs from a larger sample of 99 GRBs in Dainotti et al. (2022a). The GRBs have been observed in optical wavelengths by satellites such as Swift and the Ultraviolet/Optical Telescope (UVOT), as well as ground-based detectors such as the Subaru Telescope, the MITSuME, the reionization and Transients InfraRed telescope (RATIR), and the Gamma-Ray Burst Optical/Near-IR Detector (GROND). The sample of 99 GRBs has been fitted with a broken power law (BPL):

$$F(t) = \begin{cases} F_a \left( \frac{t}{T_a} \right)^{-\alpha_1} & t < T_a \\ F_a \left( \frac{t}{T_a} \right)^{-\alpha_2} & t \geq T_a, \end{cases} \quad (1)$$

where  $T_a$  is the break time,  $F_a$  is the flux at  $T_a$ , and  $\alpha_1$  and  $\alpha_2$  are the temporal indices for times before and after  $T_a$ , respectively. We have only selected GRBs that present a plateau, which we define as those LCs for which  $|\alpha_1| < 0.5$ . The full sample of the optical GRBs is presented in Table 1.

We take the temporal indices to be  $\alpha_2$  from the BPL fitting, as  $\alpha_2$  describes the light curve after the end of the plateau emission, which corresponds to phase III of the LC as in Zhang et al. (2006a). We consider the segment of the LC that occurs after the plateau but before the jet break. We gather  $\beta$  from the literature following the convention  $F_\nu \propto t^{-\alpha} \nu^{-\beta}$ , where  $\alpha$  is the temporal index and  $\beta$  is the spectral index. Due to the difficulty of gathering a large sample of spectral indices at the specific time  $T_a$ , we take the  $\beta$  parameter from the literature and assume a constant value throughout the LC for all GRBs in our sample. For 30 GRBs in which no optical spectral index could be found in the literature, Dainotti et al. (2022a) extrapolate the spectral index from the photon index  $\Gamma$  in X-ray (given in the Swift XRT repository, Evans et al. (2009)) by assuming  $\beta = \Gamma - 1$ . However, it cannot always be guaranteed that the X-ray and optical LCs fall in the same region of the spectral energy distribution (SED), therefore, for these GRBs, we compare the temporal index found in the optical fitting to the corresponding

temporal index found in the X-ray fitting (Srinivasaragavan et al. 2020). If the temporal indices agree within  $1\sigma$ , we can assume that the X-ray and optical LCs fall within the same region (private communication by Bing Zhang) and take the extrapolated spectral index, allowing us to retain 13 GRBs in our sample. Otherwise, we remove the GRBs from our sample. We thus remove 17 GRBs from the sample of 99, giving us a total sample of 82 GRBs.

For an example of an optical LC fitted with a BPL in our sample, please refer to Dainotti et al. (2022a). We show the distributions of the  $\alpha_1$ ,  $\alpha_2$ , and  $\beta$  parameters in our sample in Figure 1. For comparison, we also show the corresponding values of  $\alpha_2$  and  $\beta$ , as measured between the end of the plateau and the end of the LC, in X-ray wavelengths in Figure 2 for the sample of optical GRBs.<sup>9</sup>

We note that the distributions of the temporal and spectral indices differ slightly between the optical and X-ray samples. We run the Kolmogorov–Smirnov two-sample test for these distributions, finding a  $p$ -value of  $p = 0.001$ , which indicates that these distributions were not drawn from the same parent sample. However, the KS test has limitations: it is best suited for continuous distributions, it has increased sensitivity toward the center of the distribution and less toward the tails of the distribution, and sensitivity to differences in multiple characteristics between the two distributions (including location, scale, and shape). In this case, the KS test is likely to be too restrictive to provide us with critical results. Thus, we have approached the problem in a different way. Usually the distributions of GRB parameters in X-rays and optical are well fitted by Gaussian distributions (Dainotti et al. 2022 in preparation); thus we perform a less restrictive and more general test by fitting the distributions with Gaussians. The optical distribution has a mean,  $\mu = 0.75$  and a standard deviation,  $\sigma = 0.23$ , and the X-ray has  $\mu = 0.92$  with  $\sigma = 0.20$ . Thus, the difference between the X-ray and optical samples is not statistically significant—we find that the distributions are compatible within one  $\sigma$ .

## 3. Methodology

### 3.1. Analyzing CRs

Following a similar procedure to Dainotti et al. (2022, submitted), we test our sample with a set of closure relations (CRs), namely, relations between the temporal indices ( $\alpha$ ) and spectral indices ( $\beta$ ). We consider the constant-density ISM ( $k=0$ ) and stellar wind medium ( $k=2$ ) without injection presented in Tak et al. (2019) in slow-cooling (SC) and fast-cooling (FC) regimes. The CRs are defined in two regimes according to the electron spectral index  $p$ , with  $1 < p < 2$  and  $p > 2$ . The temporal and spectral indices of each GRB are plotted with their error bars. As we expect the  $\alpha$  and  $\beta$  errors to be correlated, we represent these with ellipses around the points rather than with rectangular shapes. We define the “fulfillment” of the relations as the intersection of the GRB with the CR at any point within the  $1\sigma$  ellipses.

Within our sample, we have 13 GRBs that have a spectral index extrapolated from the photon index in X-rays (orange triangles in Figure 3). It is clear that the orange points are clustered at higher values of  $\beta$ , but we consider them anyway in

<sup>9</sup> In Figure 2, we do not include GRBs observed pre-Swift (before 2005) or those not found in the XRT catalog, as the spectral index could not be computed.

**Table 1**  
Sample of 82 GRBs Used in This Analysis, Fit with a BPL

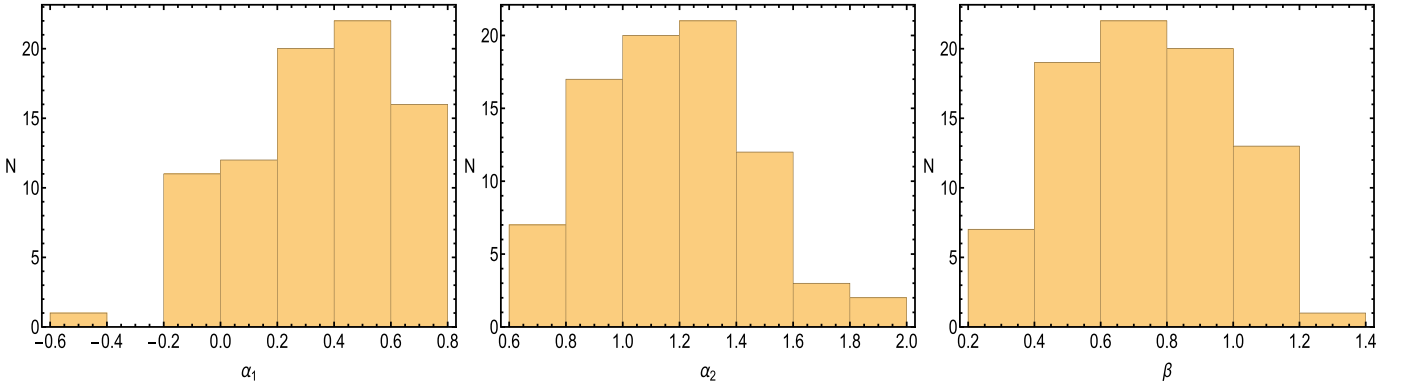
GRB	$\alpha \pm \delta_\alpha$	$\beta \pm \delta_\beta$	Author	$\beta_{\text{ref}}$	Class	$\log T_a^*$ (s)
GRB010222A	$1.25 \pm 0.08$	$0.76 \pm 0.22$	[1], [2]	[3]	L	4.24
GRB021004A	$1.38 \pm 0.03$	$0.67 \pm 0.14$	[1]	[4]	L	4.87
GRB030328A	$1.30 \pm 0.03$	$0.36 \pm 0.45$	[1]	[4]	L	3.97
GRB040924A	$1.30 \pm 0.01$	$0.63 \pm 0.48$	[1]	[4]	SN-C	3.23
GRB041006A	$1.24 \pm 0.01$	$0.36 \pm 0.27$	[5]	[3]	SN-C	3.84
GRB050319A	$0.81 \pm 0.02$	$0.74 \pm 0.42$	[6]	[4]	XRR	3.81
GRB050401A	$0.88 \pm 0.04$	$0.39 \pm 0.05$	[1], [7]	[1]	L	3.55
GRB050416A	$0.83 \pm 0.05$	$0.92 \pm 0.30$	[1]	[3]	XRF-D-IS-SN	3.93
GRB050502A	$1.89 \pm 0.21$	$0.76 \pm 0.16$	[8]	[4]	L	3.03
GRB050525A	$1.38 \pm 0.02$	$0.52 \pm 0.08$	[3]	[4]	SN-B-XRR	3.01
GRB050730A	$1.46 \pm 0.04$	$0.52 \pm 0.05$	[3]	[3]	L	3.64
GRB050801A	$1.18 \pm 0.00$	$0.69 \pm 0.34$	[3]	[4]	XRR	2.26
GRB050820A	$1.07 \pm 0.01$	$0.72 \pm 0.03$	[3], [6]	[4]	L	3.90
GRB050824A	$0.73 \pm 0.01$	$0.45 \pm 0.18$	[3]	[4]	XRF-SN-E	3.38
GRB050922C	$1.28 \pm 0.00$	$0.56 \pm 0.01$	[3], [6], [9]	[4]	IS	3.26
GRB051111A	$1.27 \pm 0.08$	$0.76 \pm 0.07$	[5]	[1]	L	2.36
GRB060124A	$0.87 \pm 0.00$	$0.73 \pm 0.08$	[6]	[10]	XRR	3.11
GRB060206A	$1.24 \pm 0.01$	$0.77 \pm 0.01$	[6]	[4]	XRR-IS	3.59
GRB060512A	$0.77 \pm 0.02$	$0.68 \pm 0.05$	[3]	[1]	XRF	3.14
GRB060526A	$1.05 \pm 0.01$	$0.65 \pm 0.06$	[3]	[4]	XRR	3.56
GRB060607A	$1.21 \pm 0.03$	$0.72 \pm 0.27$	[3]	[4]	L	2.92
GRB060708A	$0.81 \pm 0.03$	$0.88 \pm 0.05$	[11]	[12]	L	2.69
GRB060714A	$0.99 \pm 0.04$	$0.44 \pm 0.04$	[5]	[1]	XRR	3.64
GRB060729A	$1.20 \pm 0.03$	$0.67 \pm 0.07$	[6]	[4]	XRR-SN-E	4.88
GRB060904B	$1.16 \pm 0.01$	$1.11 \pm 0.10$	[3]	[4]	XRR-SN-C	3.69
GRB060927A	$1.40 \pm 0.09$	$0.86 \pm 0.03$	[3]	[1]	XRR	2.42
GRB061126A	$1.20 \pm 0.06$	$0.82 \pm 0.09$	[1], [3]	[3]	L	3.24
GRB070110A	$1.00 \pm 0.01$	$1.00 \pm 0.14$	[3]	[1]	XRR	3.91
GRB070411A	$1.34 \pm 0.09$	$1.09 \pm 0.11$	[6]	[13]	XRR	2.72
GRB070810A	$1.53 \pm 0.15$	$1.01 \pm 0.08$	[3]	[14]	XRR	3.26
GRB071003A	$1.70 \pm 0.01$	$0.35 \pm 0.11$	[3]	[3]	L	5.09
GRB071031A	$0.75 \pm 0.00$	$0.34 \pm 0.30$	[3]	[4]	XRF	2.97
GRB071112C	$0.92 \pm 0.00$	$0.44 \pm 0.11$	[4]	[4]	SN-C	2.29
GRB080310A	$1.08 \pm 0.00$	$0.42 \pm 0.12$	[6]	[4]	XRR	2.99
GRB080319C	$1.18 \pm 0.03$	$0.98 \pm 0.42$	[3]	[4]	L	2.76
GRB080330A	$1.11 \pm 0.00$	$0.42 \pm 0.15$	[3]	[4]	XRF	3.12
GRB080413A	$1.47 \pm 0.12$	$0.52 \pm 0.37$	[5]	[4]	XRR	1.35
GRB080603A	$0.95 \pm 0.02$	$0.85 \pm 0.31$	[6]	[4]	L	3.37
GRB080603B	$1.34 \pm 0.01$	$0.62 \pm 0.06$	[4]	[4]	L	3.63
GRB080605A	$0.69 \pm 0.01$	$0.57 \pm 0.35$	[4]	[4]	L	3.10
GRB080710A	$1.52 \pm 0.00$	$0.80 \pm 0.09$	[3]	[4]	L	3.74
GRB080913A	$0.90 \pm 0.13$	$1.16 \pm 0.17$	[3]	[4]	IS	4.65
GRB081203A	$1.53 \pm 0.41$	$1.08 \pm 0.02$	[15]	[11]	L	3.34
GRB090313A	$0.93 \pm 0.03$	$1.00 \pm 0.10$	[6]	[4]	XRR	2.84
GRB090423A	$0.91 \pm 0.09$	$0.45 \pm 0.13$	[3]	[4]	XRR-IS	3.73
GRB090426A	$1.17 \pm 0.02$	$0.76 \pm 0.14$	[5]	[1]	S-IS-XRR	2.01
GRB090510A	$0.96 \pm 0.14$	$0.85 \pm 0.05$	[1]	[16]	S	3.34
GRB090927A	$1.26 \pm 0.16$	$0.41 \pm 0.16$	[4]	[4]	SEE-IS	3.93
GRB091020A	$1.01 \pm 0.02$	$1.06 \pm 0.09$	[4]	[4]	L	2.15
GRB091024A	$1.53 \pm 0.03$	$0.64 \pm 0.29$	[4]	[4]	UL	3.64
GRB091127A	$1.14 \pm 0.00$	$0.43 \pm 0.10$	[5]	[1]	XRR-SN-B	4.24
GRB100418A	$1.11 \pm 0.14$	$0.98 \pm 0.09$	[5]	[11]	XRF-SN-D	4.65
GRB100513A	$1.45 \pm 1.23$	$1.20 \pm 0.10$	[17]	[13]	L	3.56
GRB100621A	$1.58 \pm 0.02$	$0.78 \pm 0.09$	[4]	[4]	XRR	3.99
GRB100906A	$1.08 \pm 0.11$	$0.84 \pm 0.22$	[1]	[4]	XRR	2.16
GRB101219B	$0.96 \pm 0.00$	$0.58 \pm 0.07$	[4]	[4]	XRR-SN-B	3.67
GRB110503A	$1.49 \pm 0.40$	$0.80 \pm 0.04$	[18]	[13]	L	4.29
GRB110715A	$1.47 \pm 0.08$	$0.90 \pm 0.22$	[4]	[4]	XRR	4.92
GRB110726A	$0.69 \pm 0.02$	$0.50 \pm 0.19$	[4]	[4]	L	2.91
GRB120119A	$1.31 \pm 0.03$	$0.89 \pm 0.01$	[5]	[11]	L	3.00
GRB120404A	$1.49 \pm 0.02$	$1.05 \pm 0.09$	[1]	[11]	XRR	3.37
GRB120711A	$1.19 \pm 0.10$	$0.53 \pm 0.02$	[16]	[16]	L	4.01
GRB120815A	$0.60 \pm 0.01$	$0.78 \pm 0.01$	[5]	[11]	L	2.73
GRB120907A	$0.87 \pm 0.16$	$0.70 \pm 0.06$	[19]	[13]	L	2.54



**Table 1**  
(Continued)

GRB	$\alpha \pm \delta_\alpha$	$\beta \pm \delta_\beta$	Author	$\beta_{\text{ref}}$	Class	$\log T_a^*$ (s)
GRB130606A	$1.23 \pm 0.03$	$0.83 \pm 0.12$	[4]	[4]	XRR	3.41
GRB130702A	$1.36 \pm 0.01$	$0.44 \pm 0.09$	[4]	[4]	SN-A-XRF	5.00
GRB140423A	$1.02 \pm 0.02$	$0.54 \pm 0.08$	[20]	[4]	L	3.55
GRB140430A	$0.80 \pm 0.02$	$1.05 \pm 0.08$	[4]	[4]	XRR	3.42
GRB140801A	$0.86 \pm 0.02$	$0.67 \pm 0.16$	[21]	[4]	L	3.83
GRB140907A	$1.00 \pm 0.08$	$1.00 \pm 0.07$	[22]	[13]	L	3.85
GRB141221A	$1.14 \pm 0.02$	$0.26 \pm 0.09$	[4]	[4]	XRR	2.42
GRB160131A	$1.25 \pm 0.56$	$0.03 \pm 0.04$	[23]	[13]	L	3.70
GRB160227A	$1.1 \pm 0.18$	$0.70 \pm 0.04$	[24]	[13]	L	3.47
GRB160804A	$1.0 \pm 0.13$	$0.90 \pm 0.07$	[25]	[13]	L	4.48
GRB161219B	$0.91 \pm 0.04$	$0.49 \pm 0.01$	[26]	[4]	L-SN-C	6.47
GRB170714A	$1.92 \pm 0.69$	$0.90 \pm 0.03$	[27]	[13]	UL	4.20
GRB180205A	$1.06 \pm 0.07$	$0.90 \pm 0.09$	[28]	[13]	L	4.63
GRB180325A	$1.37 \pm 0.11$	$1.13 \pm 0.10$	[29]	[4]	L	3.40
GRB191011A	$0.74 \pm 0.67$	$0.90 \pm 0.09$	[30]	[13]	L	2.86
GRB201020A	$1.67 \pm 0.83$	$1.10 \pm 0.11$	[31]	[13]	L	3.20
GRB970508A	$1.27 \pm 0.03$	$0.32 \pm 0.15$	[33], [3]	[4]	XRF	5.98
GRB210210A	$1.65 \pm 0.18$	$0.81 \pm 0.07$	[32]	[13]	L	3.64

**Note.** The first two columns show the  $\alpha_2$ , where  $\alpha_2$  is the distribution of the temporal index after the end of the plateau, and  $\beta$  values with their errors, the third and fourth columns show the reference for the LC and the spectral indices, respectively. The sixth column shows the class of the GRB—either long (LGRBs) or ultralong (UL); short (SGRBs), including intrinsically short (IS) and short with extended emission (SEE); X-ray flashes (XRF), X-ray rich GRBs (XRR), or GRBs with supernova (SNe) associations, classified as A, B, C, D, or E according to Hjorth et al. (2003). The seventh column shows the rest-frame time of break  $T_a^*$  found from the BPL fitting, where the \* denotes the rest frame. Data taken from Dainotti et al. (2022a), [1] Li et al. (2012), [2] Watanabe et al. (2001), [3] Kann et al. (2010), [4] Kann et al. 2022 in preparation, [5] Si et al. (2018), [6] Zaninoni et al. (2013), [7] Kamble et al. (2009), [8] Durig (2005) [9] Oates et al. (2009), [10] Misra et al. (2007), [11] Li et al. (2015), [12] Oates et al. 2022 in preparation, [13] Evans et al. (2009), [14] Schady et al. (2012), [15] de Pasquale & Parsons (2008), [16] Li et al. (2018), [17] Evans et al. (2010), [18] Frail et al. (2011), [19] Younes & Barthelmy (2012), [20] Pandey et al. (2014), [21] Kann et al. (2014), [22] Kuin & Krimm (2014), [23] Melandri et al. (2016), [24] Yoshii et al. (2016), [25] Marshall et al. (2016), [26] D’Ai et al. (2016), [27] Marshall & D’Ai (2017), [28] Emery & Evans (2018), [29] Schweyer & Kann (2018), [30] Kuin et al. (2019), [31] Kumar et al. (2020), [32] Kann et al. (2021), [33] Kann et al. (2006). For GRBs with LC data taken from multiple GCNs, please refer to Dainotti et al. (2022a) for the complete list of references.

**Figure 1.** Distribution of  $\alpha_1$  (left),  $\alpha_2$  (middle),  $\beta$  (right) for the 82 GRBs used in this study.

the analysis since the intent here is to analyze the CRs for the largest possible sample that presents optical plateau emissions. We also have 13 GRBs that have known SNe-Ib/c associations, which have more complex emissions than the FS model. We consider these 13 GRBs-SNe in the total sample as well as separately to determine their degree of fulfillment and if their behavior differs from that of the full sample. We show the full sample in Figure 3 classified according to these two considerations—GRBs with an extrapolated spectral index are shown as orange triangles, and GRBs with known SNe associations are shown as black stars. All other GRBs are shown as green circles. We keep this convention throughout the paper. We show the number and rate of the fulfillment of the CRs for the total sample in Table 2 and the GRBs-SNe in

Table 3. A visual representation of the CRs for all GRBs is shown in Figure 4.

### 3.2. Computing the 2D Luminosity–Time Correlation

For the 82 GRBs in our sample, we also compute the rest-frame isotropic luminosity  $L_a$  according to:

$$L_a = 4\pi D_L^2(z) F_a K \quad (2)$$

where  $D_L(z)$  is the luminosity distance assuming a flat  $\Lambda$ CDM cosmological model with  $\Omega_M = 0.3$  and  $H_0 = 70 \text{ km s}^{-1} \text{ Mpc}^{-1}$ .  $F_a$  is the measured optical energy flux ( $\text{erg cm}^{-2} \text{ s}^{-1}$ ) at time  $T_a$ , the end of the plateau, and  $K$  is the  $K$ -correction

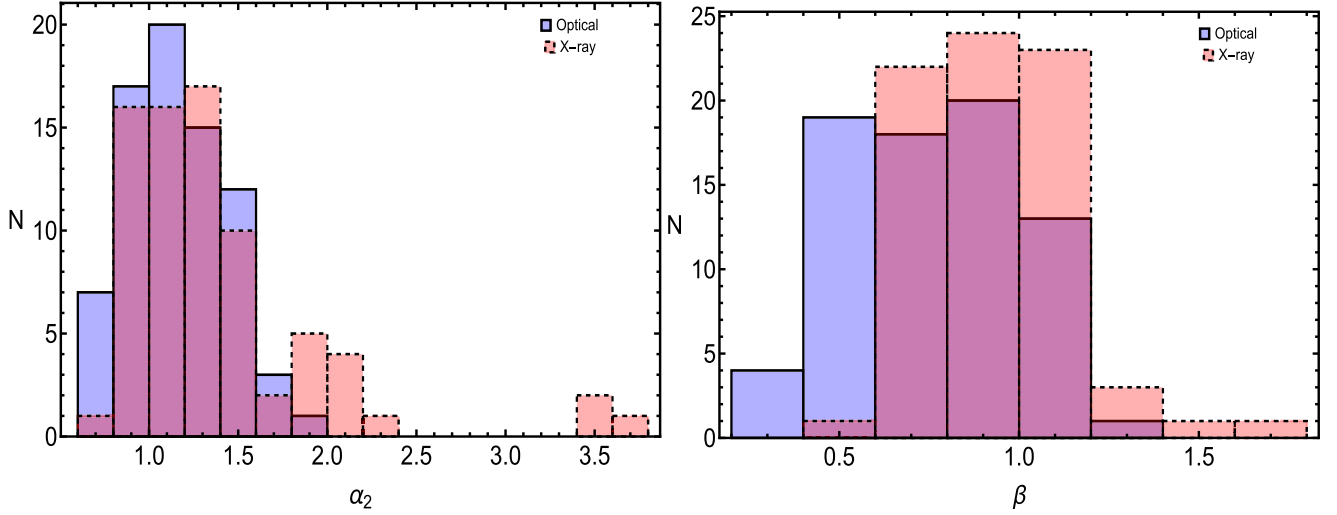


**Figure 2.** Distribution of  $\alpha_2$  (left) and  $\beta$  (right) for a sample of optical GRBs and the corresponding values in X-ray. GRBs observed pre-Swift and GRBs not found in the Swift XRT catalog are not included in the plot.

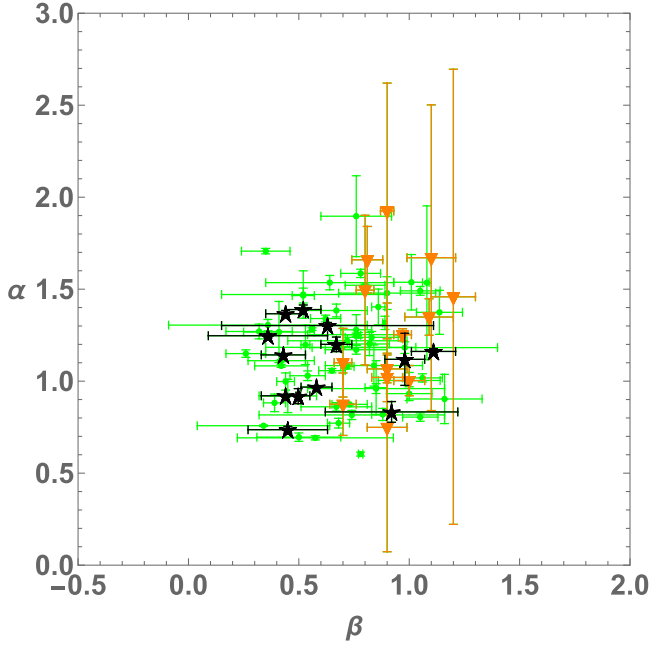


**Figure 3.** The full sample of 82 GRBs considered in this sample. GRBs with  $\beta$  extrapolated from X-rays are shown as orange triangles, while GRBs with known SNe associations are shown as black stars.

$K = 1/(1+z)^{1-\beta}$  (Bloom et al. 2001), where  $\beta$  is the optical spectral index.

We use the luminosity to develop the 2D correlation between the rest-frame end time of the plateau  $T_a^*$ , where the \* indicates the rest frame, and the luminosity at that time,  $L_a$ . The 2D relation is defined similarly to its use in other wavelengths (Dainotti et al. 2020a, 2022a):

$$\log L_a = c + a \times \log T_a^* \quad (3)$$

where  $a$  is the slope of the correlation and  $c$  is the normalization constant.

We consider this correlation for the samples of GRBs that fulfill a CR following Srinivasaragavan et al. (2020); Dainotti et al. (2021b) to determine if the intrinsic scatter of the optical correlation can be reduced by GRBs that follow a particular CR.

The correlation is analyzed under two conditions, both before and after correction for selection bias and redshift evolution. To apply this correction, we use the Efron & Petrosian (Efron & Petrosian 1992, 1995) method to remove the evolution of the data with redshift and recover the intrinsic behavior of the data. This method has been extensively tested in previous GRB studies. (Dainotti et al. 2013a, 2015a, 2015b, 2017a, 2017b, 2020a, 2021a, 2022a, 2022b, 2022d; Dainotti & Del Vecchio 2017; Levine et al. 2022).

## 4. Results

### 4.1. Optical Closure Relations

We see that the greatest rates of fulfillment are within the  $\nu > \max\{\nu_c, \nu_m\}$  regime, with 19 GRBs fulfilling the CR for  $k=0$  and 18 GRBs fulfilling the CR for  $k=2$  (Table 2). The second-most-preferred regime for the CRs is the SC,  $\nu_m < \nu < \nu_c$  regime, with 2 GRBs fulfilling the CR for  $k=0$  and one GRB fulfilling the CR for  $k=2$ . The least-preferred regime is the FC,  $\nu_c < \nu < \nu_m$ , with 0% fulfillment for both values of  $k$ . In all CRs tested, we see no strong preference for either the ISM or wind medium.

We show the plots of the CRs and fulfilling GRBs in Figure 4. The CRs are represented by either a line or a point, depending on the CRs of  $\alpha$  and  $\beta$ . CRs (either lines or points) for  $1 < p < 2$ , are shown in blue, while relation lines or points for  $p > 2$  are shown in red. The GRBs which fulfill the CRs are in purple, while those that do not are shown in green.

It is important to note that the regimes with constant values of  $\beta$  are less-preferred over those with varying  $\beta$ , as those with constant  $\beta$  would be represented by a point rather than a line and are therefore less likely to intersect multiple GRBs. Additionally, these single points are not centrally located within the GRB distribution on the  $\alpha - \beta$  plane, instead falling at the edge of the observed distribution. This suggests that, even though the single-point CRs are mathematically disadvantaged relative to the other CRs that are extended lines, there is also physical/statistical evidence that they hardly match the GRB set.

For the 13 GRBs-SNe (Table 3), we see that none of the GRBs fulfill either the SC-only or FC-only CRs in either the ISM or wind environments. The most-preferred regime remains

**Table 2**  
Table Describing Fulfillment of CRs by the Sample of 82 Optical GRBs

No Energy Injection								
$n(r)$	Cooling	$\nu$ Range	$\beta(p)$	CR: $1 < p < 2$	CR: $p > 2$	GRBs	Proportion	Figure
$r^0$	Slow	$\nu_m < \nu < \nu_c$	$\frac{1}{3}$	$\frac{6\beta + 9}{16}$	$\frac{3\beta}{2}$	2	2.44 %	(1a)
$r^{-2}$	Slow	$\nu_m < \nu < \nu_c$	$\frac{1}{3}$	$\frac{2\beta + 9}{8}$	$\frac{3\beta + 1}{2}$	1	1.22%	(1c)
$r^0$	Fast	$\nu_c < \nu < \nu_m$	$\frac{1}{2}$	$\frac{\beta}{2}$	$\frac{\beta}{2}$	0	0%	(-)
$r^{-2}$	Fast	$\nu_c < \nu < \nu_m$	$\frac{1}{2}$	$\frac{\beta}{2}$	$\frac{\beta}{2}$	0	0%	(-)
$r^0$	Slow/Fast	$\nu > \max\{\nu_c, \nu_m\}$	$\frac{p}{2}$	$\frac{3\beta + 5}{8}$	$\frac{3\beta - 1}{2}$	19	23.2%	(1b)
$r^{-2}$	Slow/Fast	$\nu > \max\{\nu_c, \nu_m\}$	$\frac{p}{2}$	$\frac{\beta + 3}{4}$	$\frac{3\beta - 1}{2}$	18	22.0%	(1d)

**Note.** The number of GRBs fulfilling the CR, the cooling regime, the frequency range, the spectral index, the CRs, the proportion compared to the total sample, and the percentage of the total sample fulfilling each relation are given.

**Table 3**  
Fulfillment of CRs by the Sample of 13 Optical GRBs with SNe Associations

No Energy Injection for SNe-associated GRBs							
$n(r)$	Cooling	$\nu$ Range	$\beta(p)$	CR: $1 < p < 2$	CR: $p > 2$	GRBs	Proportion
$r^0$	Slow	$\nu_m < \nu < \nu_c$	$\frac{1}{3}$	$\frac{6\beta + 9}{16}$	$\frac{3\beta}{2}$	0	0%
$r^{-2}$	Slow	$\nu_m < \nu < \nu_c$	$\frac{1}{3}$	$\frac{2\beta + 9}{8}$	$\frac{3\beta + 1}{2}$	0	0%
$r^0$	Fast	$\nu_c < \nu < \nu_m$	$\frac{1}{2}$	$\frac{\beta}{2}$	$\frac{\beta}{2}$	0	0%
$r^{-2}$	Fast	$\nu_c < \nu < \nu_m$	$\frac{1}{2}$	$\frac{\beta}{2}$	$\frac{\beta}{2}$	0	0%
$r^0$	Slow/Fast	$\nu > \max\{\nu_c, \nu_m\}$	$\frac{p}{2}$	$\frac{3\beta + 5}{8}$	$\frac{3\beta - 1}{2}$	2	15.4%
$r^{-2}$	Slow/Fast	$\nu > \max\{\nu_c, \nu_m\}$	$\frac{p}{2}$	$\frac{\beta + 3}{4}$	$\frac{3\beta - 1}{2}$	2	15.4%

**Note.** The number of GRBs fulfilling the CR, the cooling regime, the frequency range, the spectral index, the equations of the CRs, the proportion compared to the total sample, and the percentage of the total sample fulfilling each relation are given.

the  $\nu > \max\{\nu_c, \nu_m\}$  regime, with the same 2 GRBs fulfilling the CR in both density profiles. We observe no particular clustering of the GRBs-SNe within our data, but the GRBs with extrapolated spectral indices lie at higher values of  $\beta$  and have larger error bars.

#### 4.2. Comparing to CRs in Other Wavelengths

We can compare our results in optical to previous results obtained in X-rays and  $\gamma$ -rays to better understand the fulfillment of the standard fireball model among different wavelengths. We find 46 GRBs in our optical sample that are coincident with the sample of 222 X-ray GRBs from Srinivasaragavan et al. (2020), and 2 GRBs that are coincident with the sample of 86  $\gamma$ -ray GRBs from the Second Fermi-LAT GRB Catalog, as analyzed in Dainotti et al. (2022, submitted). We compare the results obtained in optical to the results of analyzing the CRs in X-rays (using Table 1 from Srinivasaragavan et al. (2020), taken from Racusin et al. (2009)) and  $\gamma$ -rays (using Table 3 from Dainotti et al. (2022, submitted), also taken from Racusin et al. (2009)). We summarize the results in Table 4 below.

In all wavelengths, we see that none of the coincident GRBs satisfy the fast-cooling,  $\nu_c < \nu < \nu_m$  in either the ISM or wind environments. The SC,  $\nu_m < \nu < \nu_c$  environment is

only satisfied by one coincident GRB, 090927A, for the wind environment in optical wavelengths. Most coincident GRBs satisfy the  $\nu > \max\{\nu_c, \nu_m\}$  regime in either X-ray or optical wavelengths, which is consistent with our expectations. GRBs 060904B, 070110A, 091020A, 100418A, 100513A, and 160804A satisfy this regime for both X-ray and optical in both the ISM and wind environments, while GRB 050319A satisfies this regime in both X-ray and optical in the ISM environment only. One GRB is in common with our optical sample and the  $\gamma$ -ray sample in Dainotti et al. (2022, submitted), GRB 120711A, which does not fulfill any CR in either optical or  $\gamma$ -ray wavelengths.

Only one GRB among our samples, 090510A, is found in all three wavelengths. In X-ray and optical wavelengths, this GRB does not satisfy any of the given CRs. In high energy, we see that GRB 090510A fulfills two relations, corresponding to the  $\nu > \max\{\nu_c, \nu_m\}$  regime and the ISM, SC,  $\nu_m < \nu < \nu_c$ . The fulfillment of these regimes in high energy agrees with expectations from previous studies, as the  $\nu > \max\{\nu_c, \nu_m\}$  regime and the SC,  $\nu_m < \nu < \nu_c$  are the most commonly fulfilled regions. This analysis, as given in Dainotti et al. (2021c), has been performed by fitting the LC with a Willingale et al. (2007) model and a time-sliced analysis for the spectral fitting from the time at the end of the plateau and the end time

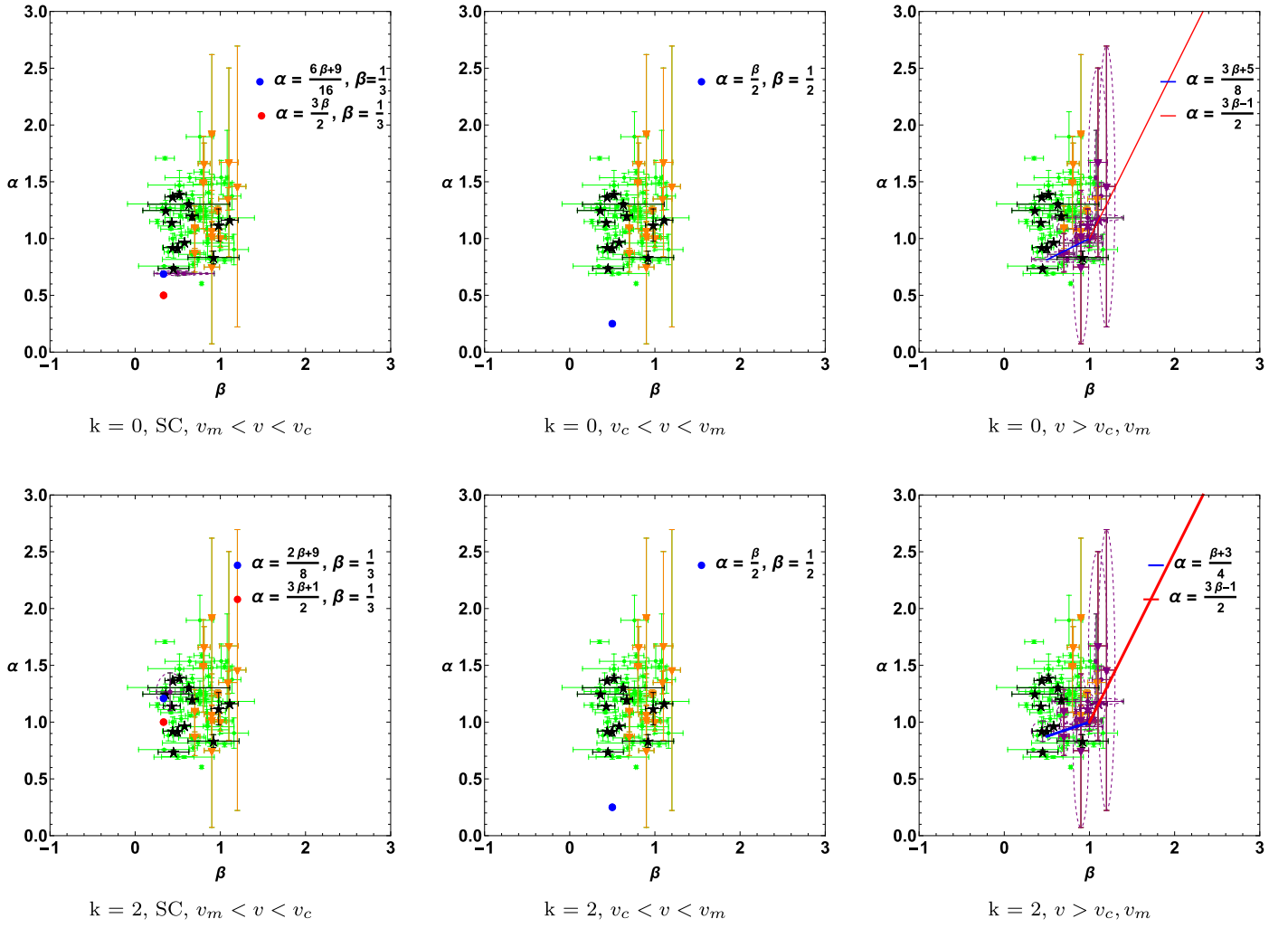


**Figure 4.** CRs from the FS model for  $k = 0, 2$  without energy injection. The relations for  $1 < p < 2$  are shown in blue, while the relations for  $p > 2$  are shown in red. GRBs that satisfy the relations are shown in purple; SNe-associated GRBs are shown as black stars, GRBs with spectral indices extrapolated from X-ray are shown as orange triangles, and other GRBs are shown in green.

of the observations. Dainotti et al. (2022, submitted) performed a similar analysis while using a BPL and takes the resulting temporal index and spectral index from the Second Fermi-LAT GRB Catalog. This gives differences in the end time of the plateau and the spectral index, which ultimately leads to different results.

We note that the distributions of the temporal and spectral indices differ slightly between the optical and X-ray samples. We run the Kolmogorov–Smirnov two-sample test for these distributions, finding a  $p$ -value of  $p = 0.001$ , which indicates that these distributions were not drawn from the same parent sample. However, the KS test has limitations, including increased sensitivity toward the center of the distribution and less toward the tails of the distribution, and sensitivity to differences in multiple characteristics between the two distributions (including location and shape). In this case, the KS test is likely to be too restrictive to provide us with useful results. Thus, we have approached the problem in a different way. Usually the distributions of GRB parameters in X-rays and optical are well fitted by Gaussian distributions (Dainotti et al. 2022 in preparation); thus we perform a less restrictive and more general test by fitting the distributions with a tool in Mathematica called FindDistributionParameters which provides the best-fit distributions. As a result, we obtain that the

best-fit distributions are Gaussians. The optical distribution has a mean,  $\mu = 0.75$  and a standard deviation,  $\sigma = 0.23$ , and the X-ray has  $\mu = 0.92$  with  $\sigma = 0.20$ . Thus, the difference between the X-ray and optical samples is not statistically significant—when we fit both distributions with a Gaussian. Therefore, we find that the distributions are compatible within one  $\sigma$ .

#### 4.3. Optical 2D Luminosity–Time Correlation

To better understand how the CRs relate to other physical parameters of GRBs, we examine the 2D Dainotti correlation for the sample of optical GRBs which fulfill the most-favored regime in our set of CRs. Following the approach of Del Vecchio et al. (2016), we investigate the distribution of  $\alpha$  values among the correlation for the full sample of 82 GRBs to determine if there is any clustering around particular values of  $\alpha$  in the  $L_a$ - $T_a^*$  relation. We see that the highest value of  $\alpha$  corresponds to a  $\log L_a$  of  $\approx 44.5$  erg s $^{-1}$  and a  $\log T_a^*$  of  $\approx 4$  s, while the lowest value of  $\alpha$  corresponds to a  $\log L_a$  of  $\approx 46.5$  erg s $^{-1}$  with a  $\log T_a^*$  of  $\approx 2.5$  s. We do not observe any particular clustering within this correlation for any values of  $L_a$  or  $T_a^*$ , indicating the temporal index does not have a significant impact on the correlation itself.



**Table 4**  
Fulfillment of CRs in X-ray, Optical, and  $\gamma$ -ray Wavelengths for Coincident GRBs

GRB	Wavelength	ISM			Wind		
		SC	FC	$\nu > \max\{\nu_c, \nu_m\}$	SC	FC	$\nu > \max\{\nu_c, \nu_m\}$
050319A	O, X	...	...	O, X	...	...	...
050401A	O, X	...	...	X	...	...	X
050416A	O, X	...	...	...	...	...	...
050730A	O, X	...	...	...	...	...	...
050820A	O, X	...	...	X	...	...	X
050824A	O, X	...	...	X	...	...	X
050922C	O, X	...	...	X	...	...	X
060124A	O, X	...	...	O	...	...	...
060206A	O, X	...	...	X	...	...	X
060526A	O, X	...	...	X	...	...	X
060607A	O, X	...	...	...	...	...	...
060708A	O, X	...	...	X	...	...	X
060714A	O, X	...	...	X	...	...	X
060729A	O, X	...	...	...	...	...	...
060904B	O, X	...	...	O, X	...	...	O, X
060927A	O, X	...	...	...	...	...	...
070110A	O, X	...	...	O, X	...	...	O, X
070810A	O, X	...	...	...	...	...	X
071003A	O, X	...	...	X	...	...	...
080310A	O, X	...	...	...	...	...	...
080319C	O, X	...	...	O	...	...	O
080710A	O, X	...	...	...	...	...	...
081203A	O, X	...	...	O	...	...	O
090423A	O, X	...	...	...	...	...	O
090426A	O, X	...	...	X	...	...	X
090510A	O, X, $\gamma$	...	...	O	...	...	O
090927A	O, X	...	...	X	O	...	X
091020A	O, X	...	...	O, X	...	...	O, X
091127A	O, X	...	...	...	...	...	...
100418A	O, X	...	...	O, X	...	...	O, X
100513A	O, X	...	...	O, X	...	...	O, X
100621A	O, X	...	...	...	...	...	...
100906A	O, X	...	...	O	...	...	O
101219B	O, X	...	...	...	...	...	...
110503A	O, X	...	...	...	...	...	...
110715A	O, X	...	...	X	...	...	X
120404A	O, X	...	...	...	...	...	...
120711A	O, $\gamma$	...	...	...	...	...	...
120907A	O, X	...	...	O	...	...	O
130606A	O, X	...	...	...	...	...	...
140423A	O, X	...	...	X	...	...	X
140430A	O, X	...	...	X	...	...	...
160227A	O, X	...	...	...	...	...	O
160804A	O, X	...	...	O, X	...	...	O, X
161219B	O, X	...	...	...	...	...	...
170714A	O, X	...	...	...	...	...	...
180205A	O, X	...	...	X	...	...	X

**Note.** Column 1 gives the name of the GRB in the optical sample that has also been analyzed in either X-rays or  $\gamma$ -rays. Column 2 gives the wavelengths for which a particular GRB has been analyzed—O for optical, X for X-rays, and  $\gamma$  for  $\gamma$ -rays. Columns 3, 4, and 5 mark whether a GRB satisfies the given CR in the ISM ( $k = 0$ ) environment, while columns 6, 7, and 8 mark whether a particular GRB satisfies the given CR in the wind ( $k = 2$ ) environment. Columns are marked with X, O, or  $\gamma$  to represent whether the relation has been satisfied in X-ray, optical, or  $\gamma$ -ray wavelengths; “...” is placed in all columns for which the GRB does not satisfy the given relation.

This result is different from the one of Del Vecchio et al. (2016), who examined the distribution of the  $\alpha$  parameters along the luminosity–time correlation for a sample of 176 GRB afterglows and found that the  $\alpha$  parameters varied systematically with luminosity within the correlation. We do not find this result in our sample; however, we note that Del Vecchio et al. (2016) used a larger sample of GRBs in X-ray

wavelengths instead of optical, which may contribute to the observed differences.

We also examine the correlation color coded by SNe association or X-ray extrapolation in the spectral index to determine if there is any clustering observed. We see that the GRBs–SNe tend to have lower luminosities and larger  $T_a^*$  than the other GRBs, located mainly at the lower end of the correlation. This may be because SNe have been observed at

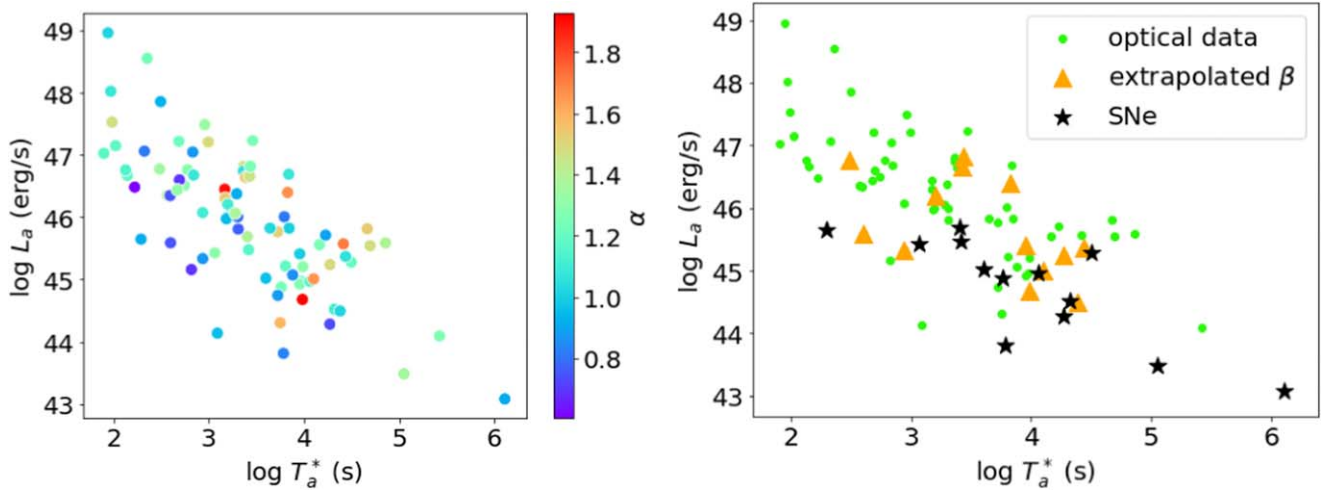


**Figure 5.** Left: the luminosity–time correlation for the full sample of 82 GRBs, color coded by  $\alpha$  value for each GRB. Right: the luminosity–time correlation for the full sample of 82 GRBs, color coded by class—SNe-associated GRBs are shown as black stars, GRBs with spectral indices extrapolated from X-ray are shown as orange triangles, and all other GRBs are shown as green circles.

**Table 5**  
Best-fit Parameters for the 2D Luminosity–Time Correlation for the Most-favored Regime in Each Set of CRs

Best-fit Parameters for No Injection, $\nu > \max\{\nu_c, \nu_m\}$ Regime							
Uncorrected for Evolution				Corrected for Evolution			
Class	N	$a$	$c$	$\sigma_{\text{int}}^2$	$a'$	$c'$	$\sigma_{\text{int}}'^2$
$k = 0$	19	$-1.05 \pm 0.30$	$49.51 \pm 1.03$	$0.92 \pm 0.18$	$-0.93 \pm 0.23$	$48.24 \pm 1.00$	$0.75 \pm 0.16$
$k = 2$	18	$-1.10 \pm 0.28$	$49.16 \pm 1.13$	$0.92 \pm 0.20$	$-0.97 \pm 0.24$	$48.36 \pm 1.06$	$0.78 \pm 0.15$

lower redshifts than other GRBs that present an optical plateau. There is no observed clustering of GRBs with extrapolated spectral indices, which are scattered within the middle of the distribution.

The correlation of the full sample of 82 GRBs, colored according to the temporal index, is shown in the left panel of Figure 5. We do not present the same analysis for  $\beta$  values as the spectral index is intrinsically correlated with luminosity by definition (see Equation (2)). For completeness of the discussion, the correlation of the full sample color coded by SNe association and extrapolated spectral index is shown in the right panel of Figure 5.

For the most-favored regime in the set of CRs, we find the 2D luminosity–time correlation for the set of GRBs that satisfies each CR to determine if the scatter can be reduced from that found in Dainotti et al. (2022a). We use the Bayesian D’Agostini method and the `cobaya` package in Python to find the best-fit parameters for each of these samples, and analyze the correlation before and after correction for selection bias and redshift evolution. The results are shown in Table 5, which presents the slope of the correlation  $a$ , the normalization parameter  $c$ , and the intrinsic scatter  $\sigma_{\text{int}}^2$ . The left columns show the parameters before correction, while the right columns show the parameters after correction (denoted with a superscript  $'$ ). As the BPL model requires four parameters to fit the LCs, we require at least four data points to fit the correlation; thus we only include the regimes and density profiles with  $> 4$  GRBs fulfilling the CRs.

We find all parameters agree within  $1\sigma$  both before and after correction. We also see that the intrinsic scatter agrees with that of the correlation for the total optical sample from

Dainotti et al. (2022a) within  $1\sigma$  for both correlations derived from the samples fulfilling both CRs before correction. After correction, the constant-density ISM ( $k = 0$ ) correlation still agrees within  $1\sigma$ , while the correlation derived from the sample fulfilling the wind medium ( $k = 2$ ) CR agrees with the intrinsic scatter of the total optical sample within  $2\sigma$ . The scatter of the correlations is reduced after correction by 18% for the ISM and 15% for the wind medium, however, we see that on average, the scatter is greater than that found in Dainotti et al. (2022a). Indeed,  $\sigma_{\text{int}}^2 = 0.74$  in Dainotti et al. (2022a) versus  $\sigma_{\text{int}}^2 \approx 0.90$  in our study before correction, and  $\sigma_{\text{int}}'^2 = 0.57$  in Dainotti et al. (2022a) versus  $\sigma_{\text{int}}'^2 \approx 0.80$  in our study after correction. A plot showing the distribution of parameters from the D’Agostini fitting is shown in Figure 6 for the correlation built with the 19 GRBs fulfilling the ISM environment in the  $\nu > \max\{\nu_c, \nu_m\}$  regime after correction, which has the smallest intrinsic scatter.

It is important to note that the sample size affects these results, especially when considering the correction for selection bias. The correlations fitted in Dainotti et al. (2022a) were found using the entire sample of 99 GRBs, whereas the results here are found using a maximum of 19 GRBs. For the correlations that have been corrected for evolutionary effects, the large scatter is, again, largely due to the small sample size—the Efron & Petrosian method requires a large sample size to work effectively, so the correction applied to the correlations here is based on the larger optical sample given in Dainotti et al. (2022a). We also note that the 3D correlation between  $L_a$ ,  $T_a^*$ , and the peak luminosity  $L_{\text{peak}}$  considered in Dainotti et al. (2022a) is not studied here as the subsample of GRBs with observed  $L_{\text{peak}}$  is too small to test additional results.

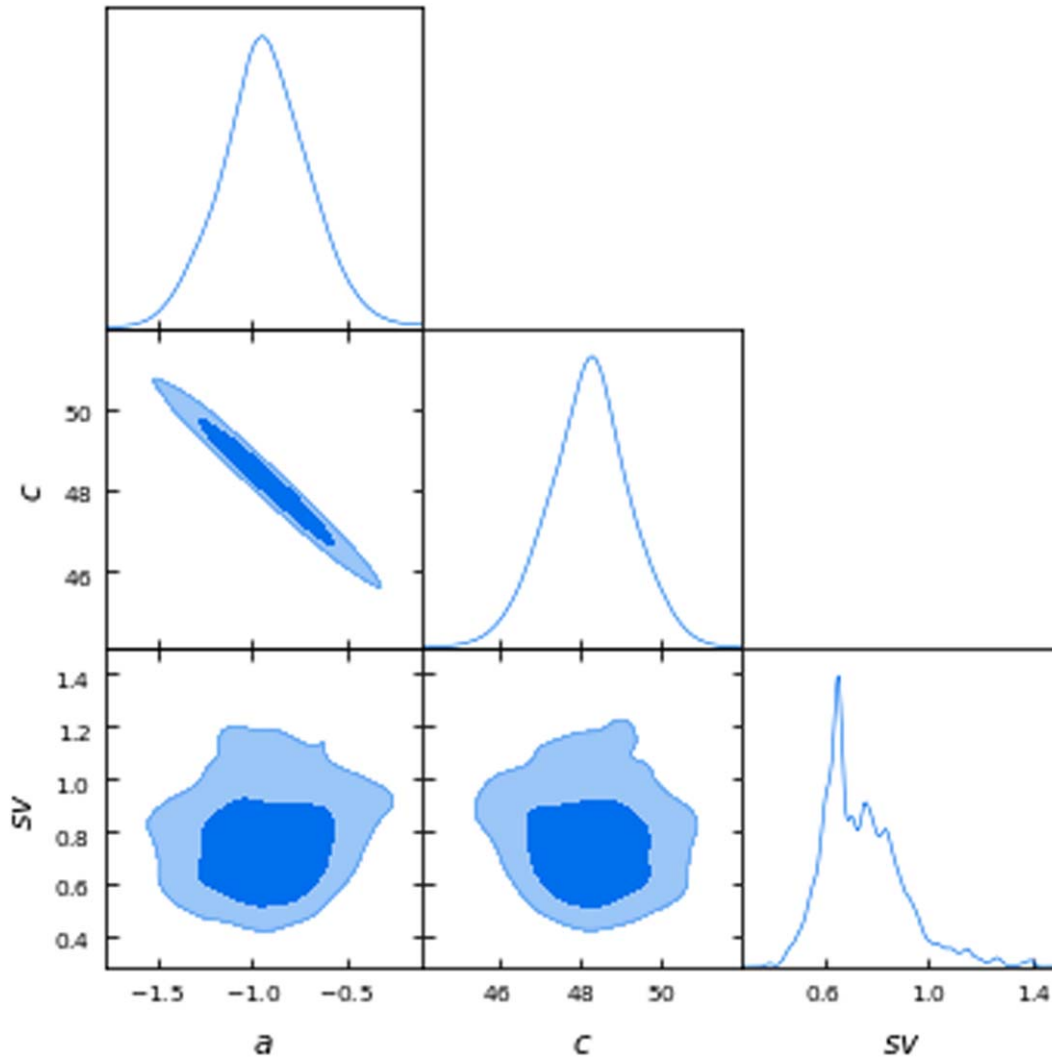


**Figure 6.** A cornerplot showing the distribution of best-fit parameters from the 2D fitting of the ISM environment ( $k=0$ ) after correction, which has the lowest intrinsic scatter.

## 5. Discussion and Conclusion

We have tested a complete set of CRs, taken from Tak et al. (2019); Racusin et al. (2009), and Dainotti et al. (2022, submitted), on a set of 82 GRBs observed in optical wavelengths and fitted with a BPL. We see that only 24/82 GRBs fulfill a CR in our sample, suggesting that our sample does not fulfill the expectation of the standard fireball model. The most-favored environment for our set of CRs is the  $\nu > \max\{\nu_c, \nu_m\}$  regime, with 23.2% fulfillment for  $k=0$ . The  $k=2$  CR in this regime shows 22% fulfillment, indicating high preference (comparatively) for this regime, but not favoring either the ISM or wind environments. We see no fulfillment for the FC-only regime for either environment, indicating a very low preference for this regime. This lack of preference may occur because the FC-only relations have constant  $\beta$ , which means their CRs are points, rather than lines as in the  $\nu > \max\{\nu_c, \nu_m\}$  regime.

We now compare our results with previous results in the literature. Oates et al. (2012) examined a sample of 48 optical LCs observed by Swift and tested whether a correlation between the luminosity and the optical decay index after 200 s could be explained by the standard model. They tested three

CRs in frequency ranges without injection -  $\nu_c < \nu_{\text{opt}}$ ,  $\nu_m < \nu_{\text{opt}} < \nu_c$  in a wind medium, and  $\nu_m < \nu_{\text{opt}} < \nu_c$  in a constant-density medium, of which we consider both  $\nu_m < \nu_{\text{opt}} < \nu_c$  regimes. They found no particular clustering of the  $\alpha$  and  $\beta$  parameters around a specific CR, indicating that the afterglows of those optical GRBs are not well explained by the basic standard model. Our results agree with this study, as many of the GRBs in our sample do not agree with the tested CRs, which would indicate the standard model is not the optimal explanation for these optical GRBs. Regarding specific CRs, the authors found  $\approx 6$  GRBs satisfying the  $\nu_m < \nu_{\text{opt}} < \nu_c$ ,  $k=0$  CR, where we find 2 GRBs, and  $\approx 4$  GRBs satisfying the  $\nu_m < \nu_{\text{opt}} < \nu_c$ ,  $k=2$  CR, where we find 1 GRB. The difference in these results may be because Oates et al. (2012) used the slope of the LC after 200 s, while we use the slope after the end time of the plateau emission, and the sample size and GRBs are different. However, regardless of these differences, we agree that a more complex model of the afterglow, including the modeling of continuous energy injection, could give a better explanation of the optical afterglow and this sample of GRBs.

Continuing on the comparison with other studies, but in different wavelengths, we find some discrepancies with studies

of CRs in higher energies, namely  $\gamma$ -rays and X-rays. In high energy, Tak et al. (2019) studied a sample of 59 GRBs detected by Fermi-LAT. They found that a high proportion of their sample satisfies the CRs, indicating that it can be well explained by the standard model. They found their most-preferred regimes to be the SC,  $\nu_m < \nu < \nu_c$  regime for the ISM/wind media, and the  $\nu > \max\{\nu_c, \nu_m\}$  regime for the ISM. We see in our results that the  $\nu > \max\{\nu_c, \nu_m\}$  is similarly preferred for the sample, though we see no strong preference for the ISM compared to the wind medium. We also see a similar preference for SC-only regimes over FC-only regimes, though the rates of satisfaction for SC-only regimes are lower in our optical sample than in the high-energy sample. Although in our study we are not able to exclude  $k=2$  using only the CRs, physical arguments (Granot & Sari 2002) indicate that optical observations of GRBs are unlikely to satisfy  $\nu > \nu_c$  with  $k=2$ , especially in the SC regime. Even for  $k=0$ , the assumption that  $\nu > \max\{\nu_c, \nu_m\}$  places restrictions on the parameters of the GRB.

Again in high energy, Dainotti et al. (2021c) studied three GRBs—090510, 090902B, and 160509A—and checked the fulfillment of the CRs without energy injection. The results show that an SC environment is preferred for all three GRBs, with an ISM environment preferred for GRB 090510 and a wind environment preferred for GRB 090902B and GRB 160509A.

In X-rays, Racusin et al. (2009) studied 230 GRB afterglows detected by Swift for a set of CRs with and without energy injection in a constant-density ISM or wind medium. In general, they found that the ISM is preferred over the wind environment, which agrees with our results for most cases—the ISM is very slightly preferred over wind for the SC-only regime, and in the  $\nu > \max\{\nu_c, \nu_m\}$  regime. However, for all other relations, we see no clear preference for one over the other.

Fukushima et al. (2017) used numerical models of X-ray and optical LCs, testing CRs in SC and FC regimes within an ISM environment. They applied their findings to the X-ray and optical afterglow of GRB 130427A and saw that discrepancy in the temporal decay indices between the wavelengths implies that the standard ISM model assuming a single emission component is not enough to describe the emission of this GRB.

It is worth noting that in the case of ISM, the spectral breaks evolve as  $\nu_m \propto t^{-\frac{3}{2}}$  and  $\nu_c \propto t^{-\frac{1}{2}}$ . Therefore, for late-time observations (e.g., where  $t_d$ , the deceleration time is  $\approx 10^4$  s and in this case we assume  $T_a=t_d$ ) the optical frequency is expected to be in the cooling regime  $\nu_{\text{opt}} > \max\{\nu_c, \nu_m\}$ . In this case, the magnetic microphysical parameter ( $\epsilon_B$ ) would be constrained by the following equation (Equation (11) in Sari et al. 1998, for the adiabatic regime):

$$\epsilon_B > 1.03 \times 10^{-2} \left( \frac{1+z}{1.54} \right)^{-\frac{1}{3}} n^{-\frac{2}{3}} \left( \frac{\eta}{0.2} \right)^{\frac{1}{3}} E_{\text{iso}, 51.8}^{-\frac{1}{3}} t_d^{-\frac{1}{3}} \nu_{\text{ev}}^{-\frac{2}{3}}, \quad (4)$$

where  $E_{\text{iso}}$  is the isotropic radiated energy,  $z$  is the redshift,  $\eta$  is the kinetic efficiency to convert kinetic energy to radiation, and  $n$  is the density medium. Thus, if we consider as an example GRB 060729 (Grupe et al. 2010), with  $z=0.54$ ,  $t_d=75857.8=10^{4.88}$  s,  $E_{\text{iso}}=6.7 \times 10^{51}$  erg, assuming the constant-density medium of 1 particle/cm<sup>3</sup>, and an efficiency of  $\eta=20\%$ , then we have  $\epsilon_B > 1.03 \times 10^{-2}$ . This value is

consistent with the derived ones in the afterglow synchrotron scenarios (e.g., see Santana et al. 2014).

Srinivasaragavan et al. (2020) also conducted a study on X-ray afterglows and again found a significant percentage of their sample fulfilled their relations, which disagrees with our results. However, they found that the SC-only regimes in either a wind ( $k=2$ ) or ISM ( $k=0$ ) environment were most favored and the FC-only regimes were disfavored, which agrees with our study.

Wang et al. (2015) studied a sample of 85 GRBs (as compared to our sample of 82 with only 34 GRBs in common with their sample) with X-rays and optical afterglows and found they could divide their sample into three categories based on their agreement with the CRs: 45 GRBs are compatible with the fireball model in all segments of the afterglow, 37 GRBs are compatible with the fireball model in at least one segment of the afterglow, and 3 are incompatible with the fireball model.

Comparing our results to CRs in lower energy, we conclude that our results largely agree with studies of CRs in radio as in Kangas & Fruchter (2021); Misra et al. (2021). Similar to Oates et al. (2012), both studies suggest a more complex model of GRB afterglows may be needed to accurately describe the lower-energy emission in GRB afterglows.

We again emphasize that optical afterglows present additional complications compared to high-energy emission or X-ray and radio afterglows, so the incompatibility of our results with the standard fireball model and the lack of agreement with studies in high-energy or X-ray wavelengths is not unexpected.

Regarding the search for a standard set of GRBs that could be driven by a given environment or regime, we analyze the 2D luminosity–time correlation for the sample of GRBs that fulfill the most-preferred CRs, both before and after correction for evolutionary effects. We find that the slope of the correlation agrees with  $-1$  within  $1\sigma$  for both  $k$ , both before and after correction, which is in line with our expectations from previous studies in X-ray (Dainotti et al. 2013b, 2021b; Srinivasaragavan et al. 2020), optical (Dainotti et al. 2020b, 2022a), and radio (Levine et al. 2022) wavelengths. However, we also note that the small sample sizes inhibit our ability to accurately compute the intrinsic scatter of the correlation, especially after correction. We additionally were not able to compute the scatter of the 3D fundamental plane in optical wavelengths for these GRBs due, again, to the small sample size.

We compare our results with Srinivasaragavan et al. (2020). They considered the 3D fundamental plane relation in X-rays to test if the GRBs that fulfilled particular CRs could be used to reduce the scatter of the 3D plane relation, similar to the analysis used in this study. They find that GRBs in all categories of CRs have scatters that agree with that of the “Gold” sample in X-rays within  $1\sigma$ , except for the FC-only categories. For the FC-only regimes, in both ISM and wind environments, they find that the scatter is reduced from the “Gold” sample and other samples found in the literature. Due to the paucity of our sample compared to previous studies, we analyze the 2D correlation rather than the 3D fundamental plane and compare it to the total sample rather than the Gold sample. We see that generally the scatter of each correlation agrees with the scatter of the 2D correlation for the total sample within  $1\sigma$  both before and after correction, though none of the CR groups reduce the scatter even after correction for selection bias. However, we again note that the lack of regimes with



reduced scatter, especially after correction, is likely due to the small sample sizes obtained in each regime.


In conclusion, we find:

1. Though expected, the majority of our sample does not satisfy the CRs, indicating that a more complex explanation may be needed to accurately model GRB optical afterglows.
2. For those CRs that are satisfied, we find a preference for the  $\nu > \max\{\nu_c, \nu_m\}$  regime. The FC-only regime is the least preferred. However, we here note that the  $\nu > \max\{\nu_c, \nu_m\}$  ordering is unlikely for optical wavelengths when  $k=2$ , as it would put severe restrictions on the GRB's parameters (Granot & Sari 2002).
3. For the most-preferred relations, in the majority of cases, the intrinsic scatter of the luminosity–time correlation agrees with that of the total correlation (given in Dainotti et al. (2022a)) within  $1\sigma$  both before and after correction for selection bias and redshift evolution.
4. The single-point CRs lie at the edge of the  $\alpha$ - $\beta$  distribution. In addition, they are mathematically disadvantaged, because they are singular points. This is additional evidence that the standard FS scenario in this simplified version may not be the optimal one to interpret the optical emission and more complex modeling is required.
5. The comparison among optical, X-rays and high-energy  $\gamma$ -rays for the GRBs that are in common with the sample analyzed here shows that the fulfillment of the  $\nu > \max\{\nu_c, \nu_m\}$  and the SC,  $\nu_m < \nu < \nu_c$  regimes in X-rays and  $\gamma$ -rays is the highest among all CRs. This agrees with the expectations from previous studies, as in high energy these are the most commonly fulfilled regions.

Eventually, with a larger sample of observed optical GRBs, we can reduce the uncertainty in our results and better understand the implications of these CRs with the optical data.

We would like to thank Bing Zhang for his comments while writing this paper and Aleksander Lenart for his initial work on the CR Notebook. D.L. acknowledges the support of the U.S. Department of Energy, Office of Science, and Office of Workforce Development for Teachers and Scientists (WDTS) under the Science Undergraduate Laboratory Internships (SULI) program, and the support of the Exploratory Research Fund (ERF) from the NAOJ Division of Science. N.F. acknowledges financial support from UNAM-DGAPA-PAPIIT through grant IN106521. We would also like to acknowledge the support of the NAOJ Division of Science in making this research possible.

## ORCID iDs

M. G. Dainotti  <https://orcid.org/0000-0003-4442-8546>  
D. Levine  <https://orcid.org/0000-0003-3411-6370>  
N. Fraija  <https://orcid.org/0000-0002-0173-6453>  
D. Warren  <https://orcid.org/0000-0002-3222-9059>  
S. Sourav  <https://orcid.org/0000-0002-0169-4003>

## References

Afonso, P., Greiner, J., Pian, E., et al. 2011, *A&A*, **526**, A154  
Beniamini, P., Giannios, D., & Metzger, B. D. 2017, *MNRAS*, **472**, 3058  
Beniamini, P., & Mochkovitch, R. 2017, *A&A*, **605**, 60  
Bloom, J. S., Frail, D. A., & Sari, R. 2001, *AJ*, **121**, 2879

Cannizzo, J. K., & Gehrels, N. 2009, *ApJ*, **700**, 1047  
Cannizzo, J. K., Troja, E., & Gehrels, N. 2011, *ApJ*, **734**, 35  
Cao, S., Dainotti, M., & Ratra, B. 2022a, *MNRAS*, **516**, 1386  
Cao, S., Dainotti, M., & Ratra, B. 2022b, *MNRAS*, **512**, 439  
Cardone, V. F., Capozziello, S., & Dainotti, M. G. 2009, *MNRAS*, **400**, 775  
Cardone, V. F., Dainotti, M. G., Capozziello, S., & Willingale, R. 2010, *MNRAS*, **408**, 1181  
Chevalier, R. A., & Li, Z.-Y. 2000, *ApJ*, **536**, 195  
Cucchiara, A., Levan, A. J., Fox, D. B., et al. 2011, *ApJ*, **736**, 7  
D'Ai, A., Kennea, J. A., Krimm, H. A., et al. 2016, *GCN*, **20296**, 1  
Dai, Z. G., & Lu, T. 1998, *A&A*, **333**, L87  
Daigne, F., & Mochkovitch, R. 1998, *MNRAS*, **296**, 275  
Dainotti, M. G., Cardone, V. F., & Capozziello, S. 2008, *MNRAS*, **391**, L79  
Dainotti, M. G., Cardone, V. F., Piedipalumbo, E., & Capozziello, S. 2013a, *MNRAS*, **436**, 82  
Dainotti, M. G., & Del Vecchio, R. 2017, *NewAR*, **77**, 23  
Dainotti, M. G., Del Vecchio, R., Nagataki, S., & Capozziello, S. 2015b, *ApJ*, **800**, 31  
Dainotti, M. G., De Simone, B. D., Schiavone, T., et al. 2022c, *Galax*, **10**, 24  
Dainotti, M. G., Hernandez, X., Postnikov, S., et al. 2017b, *ApJ*, **848**, 88  
Dainotti, M. G., Lenart, A. L., Fraija, N., et al. 2021b, *PASJ*, **73**, 970  
Dainotti, M. G., Lenart, A. L., Sarracino, G., et al. 2020a, *ApJ*, **904**, 97  
Dainotti, M. G., Livermore, S., Kann, D. A., et al. 2020b, *ApJL*, **905**, L26  
Dainotti, M. G., Nagataki, S., Maeda, K., Postnikov, S., & Pian, E. 2017a, *A&A*, **600**, A98  
Dainotti, M. G., Omodei, N., Srinivasaragava, G. P., et al. 2021c, *ApJS*, **255**, 13  
Dainotti, M. G., Ostrowski, M., & Willingale, R. 2011, *MNRAS*, **418**, 2202  
Dainotti, M. G., Petrosian, V., Singal, J., & Ostrowski, M. 2013b, *ApJ*, **774**, 157  
Dainotti, M. G., Postnikov, S., Hernandez, X., & Ostrowski, M. 2016, *ApJL*, **825**, L20  
Dainotti, M. G., Nielson, V., Sarracino, G., et al. 2022d, *MNRAS*, **514**, 1828  
Dainotti, M. G., Sarracino, G., & Capozziello, S. 2022b, *PASJ*, **74**, 1095  
Dainotti, M. G., Willingale, R., Capozziello, S., Fabrizio Cardone, V., & Ostrowski, M. 2010, *ApJL*, **722**, L215  
Dainotti, M. G., Young, S., Li, L., et al. 2022a, *ApJS*, **261**, 25  
Dainotti, M., Levine, D., Fraija, N., & Chandra, P. 2021a, *Galax*, **9**, 95  
Dainotti, M., Petrosian, V., Willingale, R., et al. 2015a, *MNRAS*, **451**, 3898  
Dall'Osso, S., Stratta, G., Guetta, D., et al. 2011, *A&A*, **526**, A121  
Del Vecchio, R., Dainotti, M. G., & Ostrowski, M. 2016, *ApJ*, **828**, 36  
de Pasquale, M., & Parsons, A. 2008, *GCN*, **8603**, 1  
Durig, D. T. 2005, *GCN*, **3340**, 1  
Efron, B., & Petrosian, V. 1992, *ApJ*, **399**, 345  
Efron, B., & Petrosian, V. 1995, *ApJ*, **449**, 216  
Emery, S. W. K., & Evans, P. A. 2018, *GCN*, **22396**, 1  
Evans, P. A., Beardmore, A. P., Page, K. L., et al. 2009, *MNRAS*, **397**, 1177  
Evans, P. A., Goad, M. R., Osborne, J. P., & Beardmore, A. P. 2010, *GCN*, **10751**, 1  
Fraija, N., Barniol Duran, R., Dichiaro, S., & Beniamini, P. 2019b, *ApJ*, **883**, 162  
Fraija, N., Dainotti, M. G., Ugale, S., Jyoti, D., & Warren, D. C. 2022, *ApJ*, **934**, 188  
Fraija, N., Dichiaro, S., Caligula do E. S. Pedreira, A. C., et al. 2019c, *ApJ*, **885**, 29  
Fraija, N., Dichiaro, S., Pedreira, A. C. C. d. E. S., et al. 2019a, *ApJL*, **879**, L26  
Fraija, N., Veres, P., Beniamini, P., et al. 2021, *ApJ*, **918**, 12  
Frail, D. A., Zauderer, A., & Berger, E. 2011, *GCN*, **12003**, 1  
Fukushima, T., To, S., Asano, K., & Fujita, Y. 2017, *ApJ*, **844**, 92  
Gao, H., Lei, W.-H., Zou, Y.-C., Wu, X.-F., & Zhang, B. 2013, *NewAR*, **57**, 141  
Granot, J., & Sari, R. 2002, *ApJ*, **568**, 820  
Grupe, D., Burrows, David N., Wu, Xue-Feng, et al. 2010, *ApJ*, **711**, 1008  
Hjorth, J., Sollerman, J., Moller, P., et al. 2003, *Natur*, **423**, 847  
Jelínek, M., Topinka, M., Karpov, S., et al. 2022, *A&A*, **662**, A126  
Kamble, A., Misra, K., Bhattacharya, D., & Sagar, R. 2009, *MNRAS*, **394**, 214  
Kangas, T., & Fruchter, A. S. 2021, *ApJ*, **911**, 14  
Kann, D. A., Delvaux, C., & Greiner, J. 2014, *GCN*, **16666**, 1  
Kann, D. A., de Ugarte Postigo, A., Thoen, C. C., et al. 2021, *GCN*, **29502**, 1  
Kann, D. A., Klose, S., Malesani, D., et al. 2010, *ApJ*, **720**, 1513  
Kann, D. A., Klose, S., & Zeh, A. 2006, *ApJ*, **641**, 993  
Katz, J. I., & Piran, T. 1997, *ApJ*, **490**, 772  
Kuín, N., & Krimm, H. A. 2014, *GCN*, **16791**, 1  
Kuín, N. P. M., Laha, S. L., & Swift/UVOT Team 2019, *GCN*, **26002**, 1  
Kumar, H., Stanzin, J., Bhalerao, V., et al. 2020, *GCN*, **28711**, 1  
Kumar, P., & Duran, R. B. 2010, *MNRAS*, **409**, 226  
Kumar, P., Narayan, R., & Johnson, J. L. 2008, *Sci*, **321**, 376



- Kumar, P., & Piran, T. 2000, [ApJ](#), **532**, 286
- Levine, D., Dainotti, M., Zvonarek, K. J., et al. 2022, [ApJ](#), **925**, 15
- Liang, E.-W., Zhang, B.-B., & Zhang, B. 2007, [ApJ](#), **670**, 565
- Li, L., Liang, E.-W., Tang, Q.-W., et al. 2012, [ApJ](#), **758**, 27
- Li, L., Wang, Y., Shao, L., et al. 2018, [ApJS](#), **234**, 26
- Li, L., Wu, X.-F., Huang, Y.-F., et al. 2015, [ApJ](#), **805**, 13
- Lü, H., Wang, X., Lu, R., et al. 2017, [ApJ](#), **843**, 114
- Marshall, F. E., & D’Ai, A. 2017, GCN, **21351**, 1
- Marshall, F. E., D’Avanzo, P., Kennea, J. A., et al. 2016, GCN, **19761**, 1
- Melandri, A., D’Avanzo, P., D’Elia, V., di Fabrizio, L., & Mainella, G. 2016, GCN, **18961**, 1
- Meszáros, P., & Rees, M. J. 1994, [MNRAS](#), **269**, L41
- Meszáros, P., & Rees, M. J. 1997, [ApJ](#), **476**, 232
- Metzger, B. D., Beniamini, P., & Giannios, D. 2018, [ApJ](#), **857**, 95
- Misra, K., Bhattacharya, D., Sahu, D. K., et al. 2007, [A&A](#), **464**, 903
- Misra, K., Resmi, L., Kann, D. N., et al. 2021, [MNRAS](#), **504**, 5685
- Nousek, J. A., Kouveliotou, C., Grupe, D., et al. 2006, [ApJ](#), **642**, 389
- Oates, S. R., Page, M. J., De Pasquale, M., et al. 2012, [MNRAS](#), **426**, L86
- Oates, S. R., Page, M. J., Schady, P., et al. 2009, [MNRAS](#), **395**, 490
- O’Brien, P. T., Willingale, R., Osborne, J., et al. 2006, [ApJ](#), **647**, 1213
- Paczynski, B., & Rhoads, J. E. 1993, [ApJL](#), **418**, L5
- Panaiteanu, A., & Kumar, P. 2000, [ApJ](#), **543**, 66
- Pandey, S. B., Kumar, B., & Agarwal, A. 2014, GCN, **16164**, 1
- Postnikov, S., Dainotti, M. G., Hernandez, X., & Capozziello, S. 2014, [ApJ](#), **783**, 126
- Racusin, J. L., Liang, E. W., Burrows, D. N., et al. 2009, [ApJ](#), **698**, 43
- Rea, N., Gullón, M., Pons, J. A., et al. 2015, [ApJ](#), **813**, 92
- Rees, M. J., & Mészáros, P. 1998, [ApJL](#), **496**, L1
- Ressler, S. M., & Laskar, T. 2017, [ApJ](#), **845**, 150
- Rowlinson, A., Gompertz, B. P., Dainotti, M., et al. 2014, [MNRAS](#), **443**, 1779
- Rowlinson, A., O’Brien, P. T., Metzger, B. D., Tanvir, N. R., & Levan, A. J. 2013, [MNRAS](#), **430**, 1061
- Sakamoto, T., Hill, J. E., Yamazaki, R., et al. 2007, [ApJ](#), **669**, 1115
- Santana, R., Barniol Duran, R., & Kumar, P. 2014, [ApJ](#), **785**, 29
- Sari, R., & Mészáros, P. 2000, [ApJL](#), **535**, L33
- Sari, R., Narayan, R., & Piran, T. 1996, [ApJ](#), **473**, 204
- Sari, R., & Piran, T. 1995, [ApJL](#), **455**, L143
- Sari, R., & Piran, T. 1999, [A&AS](#), **138**, 537
- Sari, R., Piran, T., & Narayan, R. 1998, [ApJL](#), **497**, L17
- Schady, P., Dwelly, T., Page, M. J., et al. 2012, [A&A](#), **537**, A15
- Schweyer, T., & Kann, D. A. 2018, GCN, **22544**, 1
- Si, S.-K., Qi, Y.-Q., Xue, F.-X., et al. 2018, [ApJ](#), **863**, 50
- Srinivasaragavan, G. P., Dainotti, M. G., Fraija, N., et al. 2020, [ApJ](#), **903**, 18
- Starling, R. L. C., Rol, E., van der Horst, A. J., et al. 2009, [MNRAS](#), **400**, 90
- Stratta, G., Dainotti, M., Dall’Osso, S., Hernandez, X., & De Cesare, G. 2018, [ApJ](#), **859**, 155
- Tagliaferri, G., Goad, M., Chincarini, G., et al. 2005, [Natur](#), **436**, 985
- Tak, D., Omodei, N., Uhm, Z. L., et al. 2019, [ApJ](#), **883**, 134
- Toma, K., Ioka, K., Sakamoto, T., & Nakamura, T. 2007, [ApJ](#), **659**, 1420
- Troja, E., Cusumano, G., Brien, P. T. O., et al. 2007, [ApJ](#), **665**, 599
- Wang, X. G., Zhang, B., Liang, E. W., et al. 2015, [ApJS](#), **219**, 9
- Warren, D. C., Dainotti, M., Barkov, M. V., et al. 2022, [ApJ](#), **924**, 40
- Watanabe, J.-I., Kinoshita, D., Komiyama, Y., et al. 2001, [PASJ](#), **53**, L27
- Willingale, R., Brien, P. T. O., Osborne, J. P., et al. 2007, [ApJ](#), **662**, 1093
- Yoshii, T., Nakajima, M., Negoro, H., et al. 2016, GCN, **19103**, 1
- Younes, G., & Barthelmy, S. D. 2012, GCN, **13721**, 1
- Zaninoni, E., Bernardini, M. G., Margutti, R., Oates, S., & Chincarini, G. 2013, [A&A](#), **557**, A12
- Zhang, B. 2007, [ChJAA](#), **7**, 1
- Zhang, B.-B., Liang, E.-W., & Zhang, B. 2007c, [ApJ](#), **666**, 1002
- Zhang, B.-B., Zhang, B., Sun, H., et al. 2018, [NatCo](#), **9**, 447
- Zhang, B., Fan, Y. Z., Dyks, J., et al. 2006b, [ApJ](#), **642**, 354
- Zhang, B., Liang, E., Page, K. L., et al. 2007a, [ApJ](#), **655**, 989
- Zhang, B., & Mészáros, P. 2001, [ApJL](#), **552**, L35
- Zhang, B., & Mészáros, P. 2004, [IJMPA](#), **19**, 2385
- Zhang, B., Zhang, B.-B., Liang, E.-W., et al. 2007b, [ApJL](#), **655**, L25
- Zhang, Z., Xie, G. Z., Deng, J. G., & Jin, W. 2006a, [MNRAS](#), **373**, 729
- Zhao, L., Zhang, B., Gao, H., et al. 2019, [ApJ](#), **883**, 97